Numerical and experimental validation of multi-physics design models for axial flux permanent magnet wind generator

Mouheb Dhifli, Hamza Ennassiri, Ferhat Chabour, Yacine Amara, Georges Barakat

Groupe de Recherche en Electrotechnique et Automatique du Havre (GREAH)
75 rue Bellot, 76058 Le Havre, France
dhifli.mouheb @ gmail.com

ABSTRACT. *An Axial Flux Permanent Magnet synchronous (AFPM) generator dedicated to small wind turbine is presented. Hence, the investigation of electromagnetic performance is done using quasi-3D analytical model based on multi-slice 2D analytical solution of Maxwell equations coupled sequentially to thermal model and mechanical model for rotor thickness study and vibration behaviour. The manufactured prototype has 10 kW rated power and operates at 375 rpm. This three-phase direct drive generator has double-stator-single-rotor configuration with 20 poles, 24 slots and modular windings. Experimental results such as Electromotive Forces (EMF) and inductances are agreed with those obtained from analytical simulation; both of them have been satisfying the desired technical specifications.*

RÉSUMÉ. *L'objectif de ce travail est de présenter un outil de conception analytique multi-physique pour la modélisation d'une génératrice synchrones à aimants permanents à flux axial. Cette approche est basée principalement sur la méthode de résolution formelle des équations de Maxwell. L'analyse des performances électromagnétiques de la machine est réalisée à l'aide d'un modèle analytique quasi-3D basé sur la technique multicouche. Cette analyse est couplée à la fois à une étude mécanique portant essentiellement sur le rotor et à un modèle thermique utilisant la méthode nodale. Afin d'évaluer la pertinence de cette approche multiphysique, un prototype de 10 kW fonctionnant à 375 tr/min est construit. Ce générateur discoïde triphasé à rotor interne à entraînement direct dispose de 20 pôles, 24 encoches et d'un bobinage dentaire. Les mesures expérimentales des grandeurs globales telles que la force électromotrice (FEM) et les inductances valident bien les modèles théoriques, à savoir le modèle éléments finis et le modèle analytique.*

KEYWORD: *design, axial flux machine, analytical solution, 3D finite element analysis, wind turbine, experimental results.*

MOTS-CLÉS : *modélisation, machine à flux axial, modèle analytique, méthode des éléments finis, génératrice, résultats experimentaux.*

DOI:10.3166/EJEE.18.27-60

1. Introduction

Since the 80s, the AFPM machine is under evolution. This machine has its own merits due to its pancake shape, compact construction and high power density (Gieras *et al.*, 2008). Also, called Disk-Type machine, it can be used for electrical vehicles, industrial equipments, and small wind turbine applications. There are several kinds of AFPM machines which had been investigated by many reviews, hence the differences, advantages, and disadvantages were discussed. (Krebs *et al.*, 2012; Mahmoudi *et al.*, 2014; Hemeida *et al.*, 2014; Seo *et al.*, 2015). This research deals with the problem of direct drive generator structures for small wind turbines. In fact, from among all permanent magnets machine based wind converter structures, the direct drive AFPM machine can be considered as an efficient candidate for the case of small wind turbine application. The choice of such structure could be justified by its special properties which are considered as the advantageous over Radial Flux Permanent Magnet (RFPM) machines in certain applications. First of all, the AFPM machines have a planar air gap. As well as, their topology is ideal for modular machine design, where the modules number is adjusted to the power or torque requirements. Thereafter, certain number of geometric constraints for low speed operations should be satisfied, like having smaller outer diameter of stator cores. The AFPM machines could then be considered as a suitable solution, as reported by (Gieras et al, 2008). In order to evaluate the performance of the AFPM machine for such applications, a 10 kW stator-rotor-stator prototype was designed (Abdel-Karim, 2008). In this context, modeling the machine is determined by contradictory requirements which are related to the computations speed (fastness) and accuracy. Indeed, due to the intrinsic 3D nature of its magnetic field distribution, the study of axial flux machines must be done using 3D magnetic modeling such as the 3D Finite Element Analysis (FEA). However, 3D FEA is highly time-consuming especially if the objective is to achieve a preliminary design of the machine. Thus, pre-design of axial flux generator was achieved thanks to analytical models. Indeed, the analytical models of electric machines are often preferred at early design stages due to their ability to reduce computation time compared to finite elements models. The FEA is always used for verification and validation of the designed machine. The developed analytical magnetic model coupled to semi-analytical thermal model, and mechanical study is used to design the 10 kW, 375 rpm, 20 poles and 24 slots (Azzouzi, 2007; Abdel-Karim, 2008; Tiegna, 2013). Then, the part of novelty in this paper beyond the synthesis of the conceptual approach is to validate and highlight the capabilities offered by those models by comparing them to 3D FEA simulations as well as to measurements of local and global quantities. Finally, the resulted measurements which are performed on the manufactured prototype were satisfactory, and meet the desired performances that were defined at the design stage. The measurements of open circuit EMFs and cyclic inductance have been compared to the analytical ones, hence good agreement was obtained.

2. AFPM wind generator

2.1. Optimised Parameters

A Genetic multi-objective Algorithm (GA) was applied to design a 10 kW AFPM machine dedicated to wind energy application (Abdel-Karim, 2008). This multiobjective optimisation algorithm is coupled to multi-physics analytical model, in order to find the best compromise solutions known as Pareto solutions for a given set of constraints reflecting the system behaviour. Different objectives are considered in this study such as "weight/efficiency", "Joule losses/PM volume", and "Power to volume ratio/efficiency". Figure 1 gives Pareto-optimal solutions where the weight and the efficiency of the generator are taken as objectives for different values of the PMs remanence B_r. Improving the efficiency by increasing B_r is clearly shown for lower efficiency values (A). Also, it could be noted that the efficiency stagnates beyond a percentage of 93% for any given remanence value (Br). This is due to the impossibility of reducing the total losses continuously. According to this figure, the interesting solutions are situated in the knee zone. Solutions outside this zone are less interesting.

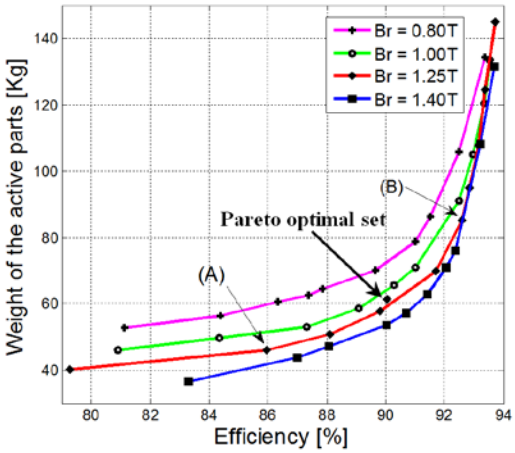

Figure 1. The Pareto set of the optimal design problem for the criterion "weight/efficiency"

Figure 2 illustrates the Pareto front where minimizing both of the PMs volume and Joule losses is taken as objective for different values of B_r. This figure clearly shows that the lowest Br value request the highest amount of PMs for a given value of Joule losses. Two particular points "C" and "D" were defined on the curve relative to $B_r = 1.25T$. The 'C' point represents the limit from which the Joule losses increase for a constant PMs volume. The 'D' point indicates the increasing of PMs

volume while the joule losses remain constant. Thus, no improvement of efficiency is possible by increasing the PMs volume. According to this analysis, the solutions between “C” and “D” points offer better compromise.

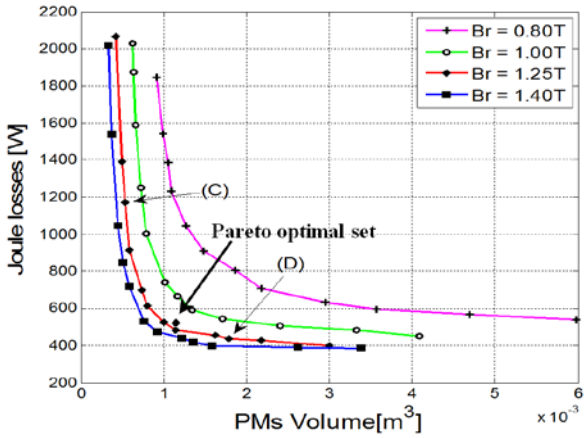

Figure 2. Pareto set for the criterion “PM volume/Joule losses”

Among the founded solutions, a compromise between the attributes and the generator performances, taking into account the criterion “weight/efficiency” which is essential for a wind turbine application. The generator weight is an important element for determining the weight of the nacelle which impacts the tower vibrations. This criterion permits the fixation of the Pareto-optimal parameters set (Table 1). Figure 3 shows the structure of the studied machine. The outer diameter should be then equal to 360 mm and the nominal speed is imposed at 375 rpm. In order to maintain the electrical frequency close to 50 Hz, the number of pole pairs is chosen equal to 10 and the number of slots-equal to 24. The use of non-overlapping-concentrated windings allows satisfying the constraint of reducing the cogging torque.

Table 1. Machine optimal parameters set

Electrical output power (kW)	10	Rated speed (rpm)	375
R_i and R_e (mm)	135 and 180	Pair poles number	10
Air gap length per stator (mm)	1	Slot number	24
Axial length (mm)	173.8	Residual induction B_r (T)	1.21
h_a, h_0 and h_s (mm)	4.7, 2 and 55	Active mass (Kg)	60.7
τ_m / τ_p (mm)	0.85	Efficiency	≥ 90%
w_s w_0 and w_a (mm)	22, 2 and 36.55	Joule losses (W)	500
Magnets distribution	Parallel (axial)	Magnets volume (m^3)	1.3

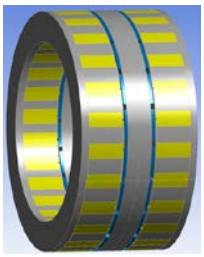

Figure 3. AFPM machine geometry

2.2. Stator

Some special modifications were adopted in order to facilitate the stators assembly. Regarding some technical difficulties and realization cost aspect, it was decided to build the stator magnetic circuit with segmented magnetic circuits (Figure 4c). Each segment is constituted of tooth and part of stator back iron, as shown in Figure 4c). These segments are then wound and bolted in the aluminium plate (Figure 4d) to form the stator magnetic circuit. Where, the inner and outer radii are equal to 135 mm, and 180 mm, respectively. This segmentation introduces supplementary air gaps when assembling the stator core. This choice was made due to the fact that the manufacturing of a one piece stator core was very expensive. This point leads to increase slightly the external radius of the machine in order to keep the same performances. However, the stator modular building simplifies the stator manufacturing by using flat laminations and by winding coils around teeth (modular windings) before assembling the stator. This results in a lower manufacturing cost.

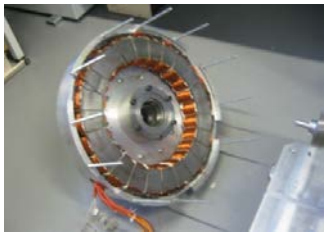

(a) external view of the stator disc

(b) external view of the rotor disc

(c) stator tooth

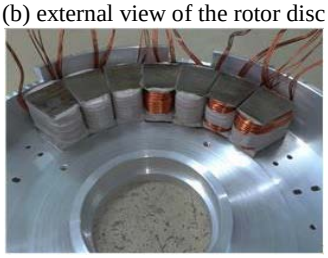

(d) stator built

Figure 4. Exploded view of the machine

2.3. Rotor

A stator-rotor-stator structure has been selected (Gieras *et al.*, 2002; Abdel Karim, 2008). This configuration has the advantage of allowing the rotor thickness reduction due to the fact that the flux passes from one stator to the other. However, due to an axial force of (20 kN), the rotor disk was made by a magnetic steel having a high elasticity limit that can resist to theses mechanical constraints. Therefore, the risk of a friction between stator and rotor disk is avoided. Finally, mechanical reinforcements are necessary to overcome the rotor torsion, flexion and stress (Figure 4b). These reinforcements and the steel disk can be provided, while their thickness is to be determined based on the desired stiffness.

2.4. Permanents Magnets

Trapezoidal permanent magnets (Figure 5) are made of neodymium-iron-boron and are glued on both surfaces of the rotor structure. Their remanent flux density is equal to 1.1 T and the magnetization is oriented in the axial direction.

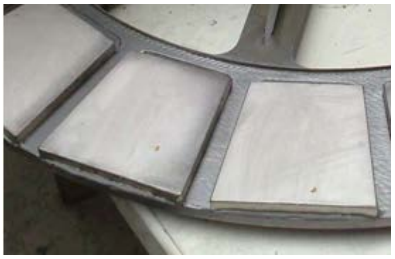

Figure 5. Overview of the magnet shape

3. Analytical modelling of the AFPM machine

In the early stages of design and optimization process the complete analytical sizing model will be useful to evaluate and analyze the machine performance with less computing time than it is in FEA.

3.1. Magnetic model

3.1.1. Quasi 3D open-circuit field

A considerable amount of literatures reporting the subsequent assumptions, which have been opted for the analysis provided. The permeability of the ferromagnetic material is considered infinite. The permeability of PMs is assumed to

be equal to that of air and their resistivity is infinite. Also, the remanence is considered to be ideal and oriented in the axial direction.

Indeed, the proposed model is based on an exact 2D solution of the magnetic field. The mathematical approach leading to the exact solution of the Maxwell's equations using the separation of variables method in the different regions is briefly exposed. Then, the global quantities expressions are derived from the solution of the magnetic field and the open circuit analytical results were compared with those obtained by FEA (Azzouzi *et al.*, 2005; Tiegna *et al.*, 2012).

Figure 6 presents the principle of the quasi-3D model. The machine is divided into certain number of annular slices in the radial direction (Figure 6a). The analytical model based on the solution of Maxwell equations is established at the average radius of each slice *(s)* (*s*=1… N_s (number of slice)) as shown in Figure 6b. The configuration shown in Figure 6e is obtained by unrolling the curved surface (Figure 6d) obtained by cutting the slice with a cylindrical plane at its mean radius (Figure 6c). With this approach, the inductions in different regions depend implicitly on the average radius of the considered slice. Thus global quantities G are carried out by summing the contributions of each layer (slice).

$$G = \sum_{s=1}^{N_C} G^{(l)} \tag{1}$$

Where, $G^{(l)}$ is the global quantity in the considered slice.

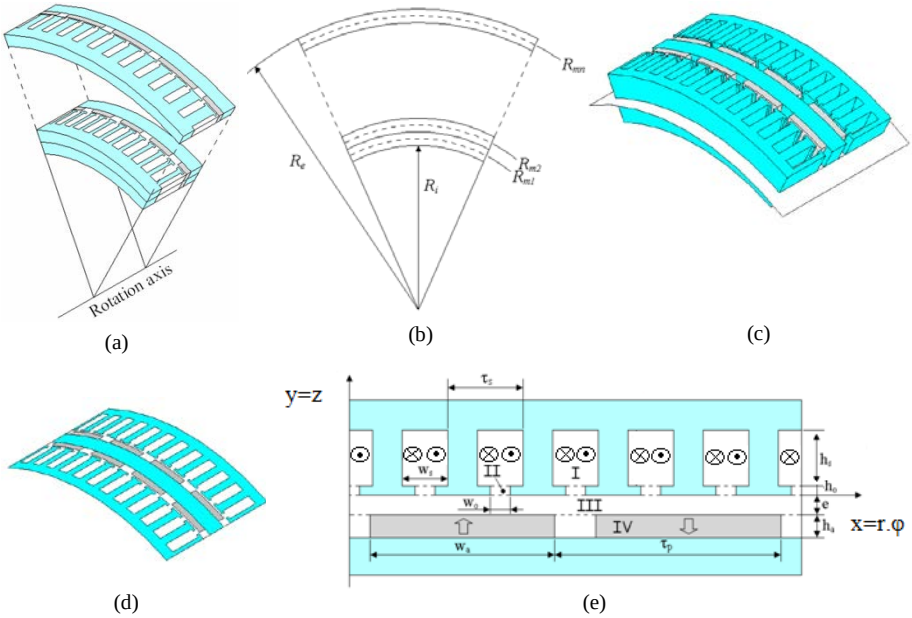

Figure 6. Field regions of idealized axial flux machine (polar coordinates)

Combining the Maxwell's equations and considering the fact that the magnetic flux density is equal to the curl of potential vector which subjects to the Coulomb gauge $\nabla \cdot \mathbf{A} = 0$, hence the partial derivative Equation (2) is obtained.

$$\Delta\mathbf{A} + \mu_0 \mathbf{J} + \mu_0 \overrightarrow{rot}\, \mathbf{M} = 0 \tag{2}$$

Where, **M** is the remanent magnetization.

The field vectors **B** and **H**, in the different regions, are coupled by:

$$\mathbf{B} = \begin{cases} \mu_0 \times \mathbf{H} & \text{in regions I, II and III} \\ \mu_0 \times (\mathbf{H} + \mathbf{M}) & \text{in region IV} \end{cases} \tag{3}$$

Taking into account the multiple assumptions mentioned above and the use of variable change $x = r \cdot \varphi$ and $y = z$ $\mathbf{A}$ has only $\mathbf{Az}$ component in Cartesian coordinate which is independent of z. It should be noticed that the $\left(o, \vec{z}\right)$axis of the Cartesian coordinate system related to the 2D model (Figure 4e) is different from the $\left(o, \vec{z}\right)$ axis corresponding to the machine rotation axis.

As well as, Equation (3) formulates the magneto static potential vector which will be written in Cartesian coordinates and solved in order to calculate the exact magnetic field distribution. Thus (2) could be rewritten in the form given by Equation (4).

$$\begin{cases} \dfrac{1}{r^2}\dfrac{\partial^2 A}{\partial \phi^2} + \dfrac{\partial^2 A}{\partial z^2} = -\mu_0 J & \text{in region I} \\ \dfrac{1}{r^2}\dfrac{\partial^2 A}{\partial \phi^2} + \dfrac{\partial^2 A}{\partial z^2} = 0 & \text{in regions II and III} \\ \dfrac{1}{r^2}\dfrac{\partial^2 A}{\partial \phi^2} + \dfrac{\partial^2 A}{\partial z^2} = \dfrac{-1}{r}\dfrac{\partial B_R}{\partial \phi} & \text{in region IV} \end{cases} \tag{4}$$

On the other hand, using the separation of variables technique and for a given slice having R_m as mean radius, the general solution of these equations can be expressed for the region 'i' by (5):

$$A^{(i)}(\phi, z) = A_p^{(i)}(\phi, z) + a_0^{(i)} + \sum_{k \neq 0} \frac{R_m}{k\lambda_p} \begin{bmatrix} C_k^{(i)} ch\left(\dfrac{k\lambda_p z}{R_m}\right) \\ + D_k^{(i)} sh\left(\dfrac{k\lambda_p z}{R_m}\right) \end{bmatrix} \cdot \begin{bmatrix} E_k^{(i)} \cos\left(k\lambda_p \phi\right) \\ + F_k^{(i)} \sin\left(k\lambda_p \phi\right) \end{bmatrix} \tag{5}$$

Where $\lambda_p = \gcd(p, N_s)$ depends on boundary conditions in each region, $C_k^{(i)}$, $D_k^{(i)}$, $E_k^{(i)}$, $F_k^{(i)}$ are the Fourier series coefficients of magnetic field in region '*i*', *i* = I, II, III, IV and A_p is the particular solution of (2).

In order to compute the Fourier series coefficients of the magnetic field, so boundary conditions between regions (interface conditions) are required. The use of these conditions yields system of equations constituted of relations in between the magnetic field Fourier coefficients in the air gap region. These interface conditions will be exploited between regions I (stator slots) and II (slots opening areas) at first, then between II and III (air gap), and finally between III and IV (PMs). Analytical solutions for magnetic vector potential and field expressions in each region were presented by the authors in (Tiegna *et al.*, 2012).

The developed model utility and accuracy would be demonstrated *via* the comparison between 3D FEA open circuit results and analytical ones. The studied structure has been first modelled using 3D FE electromagnetic model. The median plane symmetry of the structure allows reducing the studied geometry to one stator and half a rotor. Also, the greatest common divisor of the stator slots (24) and the poles (10) being equal to 2, the 3D FE magnetic computation are finally performed on the quarter of the machine geometry as shown in Figure 7. The magnetic mesh is then equal to 1251790 nodes.

The 3D finite element analyses were performed in the same conditions as the analytical model. So in order to have a like to like comparison, the relative permeability of the iron parts is high (μr=105) which explain the concordance between FE simulations and analytical ones.

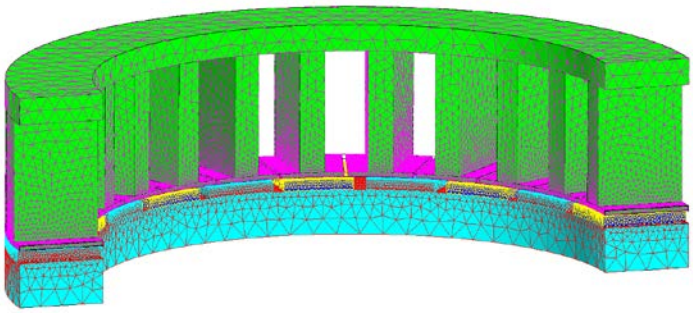

Figure 7. 3D finite element model of the AFPM generator

The solution in the middle of the air gap (normal component and tangential component) at the machine mean radius (r = R_0) for a given position of the rotor relatively to the stator are shown in Figure 8 and Figure 9. From these figures, excellent concordance is obtained between analytical model and FEA.

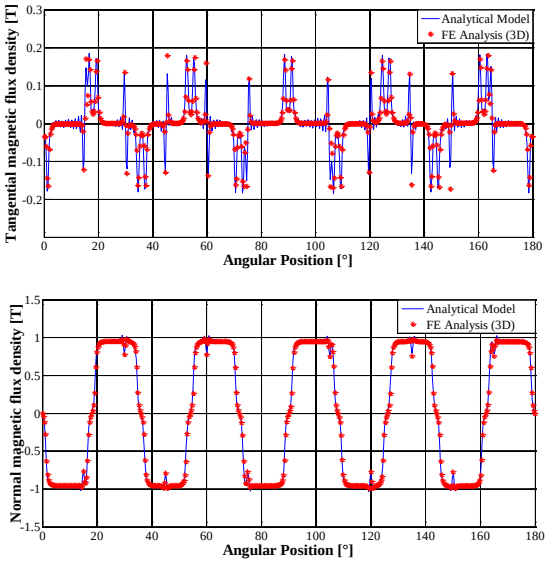

Figure 8. Comparison of open circuit magnetic flux density components in the air gap region of the machine for r = R_0 = (Ri + Re)/2; Z = -e/2

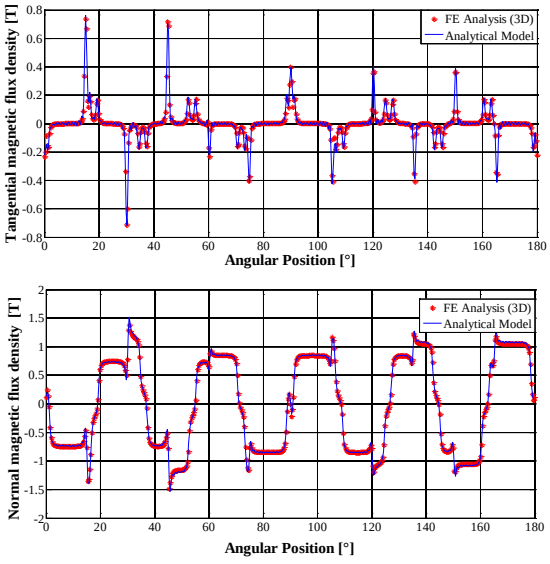

Figure 9. Comparison of induction flux density components in the air gap region of the machine at load for r = R_0 = (R_i + R_e)/2; Z = -e/2

3.1.2. Global quantities computation

The computations of flux linkage, EMF, inductances and torques are enabling the machine performance evaluation. Furthermore, global quantities can be used for the coupling of developed model with electric circuit equations. It can then be used to study behaviour of axial flux machines when connected to power converters and so for sizing and optimisation purposes. In the next subsections these global quantities will be evaluated.

3.1.2.1. Electromotive force calculation

The EMF is computed by Stokes theorem using vector potential in slots. This technique is specific to analytical models which take into account the stator slotting in explicit manner. The flux passing through the portion of coil corresponding to slice's' and located in the slots *'l'* and *'l+1'* is given by Equation (6):

$$\Phi_c^s = \frac{N_t}{h_s w_s} \int_{R_{is}}^{R_{os}} \int_{h_o}^{h_o+h_s} \left(\int_{\varphi_{1l}^{(s)}+\frac{w_s}{2}}^{\varphi_{1l}^{(s)}+w_s} A^{(I,l,s)} \cdot d\varphi - \int_{\varphi_{1(l+1)}^{(s)}}^{\varphi_{1(l+1)}^{(s)}+\frac{w_s}{2}} A^{(I,l+1,s)} \cdot d\varphi \right) dz\, dr \qquad (6)$$

Where, $A^{(I,l,s)}$ is the open circuit vector potential in slot *'l'* for the slice's' (the current density $\mathbf{J}$ must be equal to zero in (2)), R_{is} and R_{os} are the inner and outer slice radii, respectively, as well as w_s, φ_{1l} are slot opening angle, and angular coordinate of the coil first edge (middle of the slot) for the slice, respectively.

The total phase flux linkage is obtained by adding fluxes of all coils belonging to this phase, and the induced EMF per phase is calculated by differentiating the flux linkage.

3.1.2.2. Self and mutual inductances computation

As well as, in EMF calculation, the estimation of self and mutual inductances could be achieved by using the previously defined technique and substituting permanent magnets by the air. However, analytical models that do not take into account stator slotting in explicit manner; they couldn't be used to estimate the total self or mutual inductances, since slot leakage inductances couldn't be evaluated. These models could be used only to estimate air gap self (magnetizing) or mutual inductances. The slot leakage-inductance could be estimated only using separate model as suggested by (Azzouzi, 2005; Tiegna *et al.*, 2012). When, using slots potential vector, it is not necessary to divide self and mutual inductances calculation in two steps. Estimation of both inductances is performed straightaway. The air gap self and mutual inductances are deduced from the stator phase and flux linkage, which can be calculated using same formula as equation (6). In this case, $A^{(I,l,s)}$ is the potential vector due to armature reaction field (current flowing in one phase

only). In the case of slot 'l' filled with conductors of one phase, the flux passing through this coil (coil 'c' having N_t turns in series) is given by Equation (7):

$$\Phi_c = N_t \sum_{s=1}^{N_c} (R_{os} - R_{is}) \left(a_0^{(I,\,l,s)} - \frac{\mu_0}{6} J^{(l)} h_s^2 \right) \tag{7}$$

Whereas, the coefficients calculation $a_0^{(I,l,s)}$ have been elaborated in (Tiegna *et al.*, 2012). This expression must be adapted in the case of non-overlapping concentrated winding because calculation of potential vector spacial average must be done on half of each slot. If the applied current density corresponds to 1At, the coil self-inductance will be directly given by the flux passing through it. Total self-inductance is then obtained by adding inductance of all coils belonging to this phase. It should be taken into account, in the summation of fluxes, how coils are connected. Mutual inductance could be easily estimated by using the same approach. Flux passing through phase, where the flowing current should be calculated (Abdel Karim *et al.*, 2006; De la Barrière *et al.*, 2010; Tiegna *et al.*, 2011; Lubin *et al.*, 2011).

3.1.2.3. Torque calculation

Cogging torque calculation is performed using Maxwell stress tensor method. This method is applied on the surface of permanent magnets at the interface between regions III and IV. By applying Maxwell stress tensor method, torque applied on the rotor could be expressed as in Equation (8) (Zhu *et al.*, 2005; Barakat *et al.*, 2010).

$$\Gamma_{cog} = \frac{\pi}{3\mu_0} \sum_{s=1}^{N_s} \left(R_{o,s}{}^3 - R_{i,s}{}^3 \right) \times \sum_{n \neq 0} \left(C_n^{(III,s)} F_n^{(III,s)} - D_n^{(III,s)} E_n^{(III,s)} \right) \tag{8}$$

Where, $C_n^{(III,s)}$, $D_n^{(III,s)}$, $E_n^{(III,s)}$, $F_n^{(III,s)}$ are coefficients of open-circuit magnetic field solution in region III for the slice 's'.

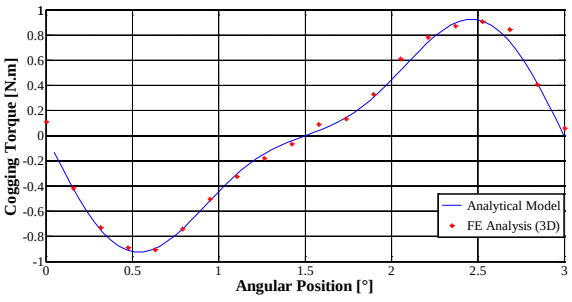

Figure 10. Comparison of Cogging torque waveforms

Figure 10 shows the wave form comparison between the single side cogging torque simulated with 10 slices in analytical model and FEA.

The electromagnetic torque is obtained by replacing the coefficients of open-circuit magnetic field solution in region III for the slice "s" by the on load coefficients given by (8). So, the comparison between FE results and analytical model results for the electromagnetic torque is exposed in Figure 11. The current density J (=3A/mm^2) combined to the non-overlapping winding may be considered to demonstrate the machine being sufficient self-ventilating.

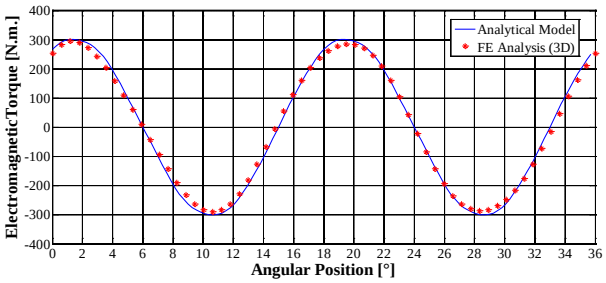

Figure 11. Comparison between the analytical model and the FEA results for electromagnetic torque

3.1.2.4. Output power

The studied AFPM machine was modeled to be integrated in a direct drive wind turbine system as shown in Figure 12.

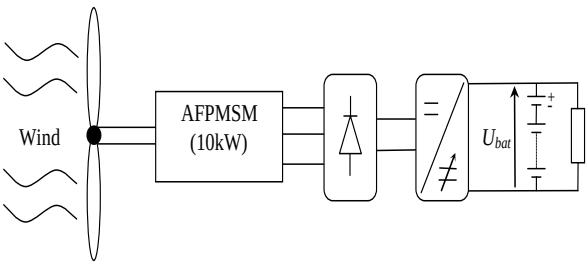

Figure 12. Presentation of the designed wind turbine system

The studied wind turbine has a diameter of 4 m and a height of 30 m and an output nominal power of 10 kW. Based on a similar commercialized wind turbine, the torque *versus* speed characteristics of the turbine is presented in Figure 13. Due to direct coupling, the maximum torque waveform versus rotational speed is directly applied to the generator shaft. For normal operation, the maximum electrical power

is obtained by controlling the rotational speed in respect to the measured wind speed. This task is done via the control of the buck-boost chopper. However, for the presented study, the machine was designed based on the rated operation point only where the chopper was replaced by its corresponding rated duty cycle. Figure 14 shows the rated electric power with respect to the rated speed. The output power is obtained by calculating the rated electromagnetic power for the rated speed and substracting the estimated rated losses.

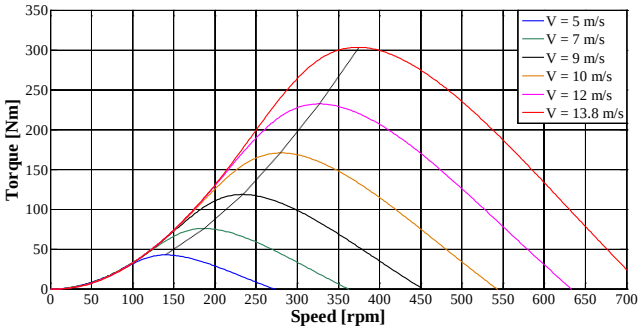

Figure 13. Torque versus *speed characteristics of the generator*

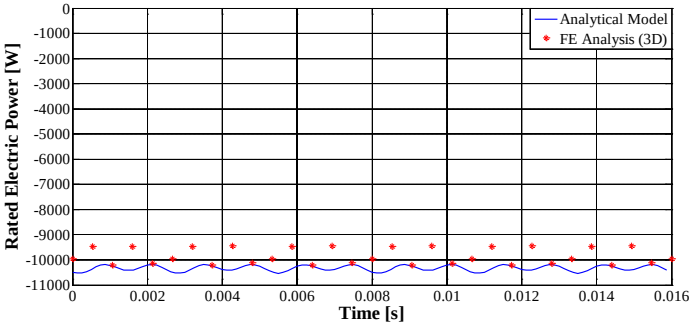

Figure 14. Comparison between the analytical model and the FEA results for electric power

3.1.2.5. CPU Time Comparison

The comparison of the CPU time computing is performed between the FEA and the analytical model. It should be noted that the duration time of both models preparation before execution (mesh and geometric construction) is not taken into account because this time depends essentially on the FE software and the analytical design tool usage expertise.

The simulation was done on core i7 processor, and 12 GB installed memory with 64 bit operating Windows 7 system. Table 2 summarizes the CPU time computing and compares the FEA with the analytical model (Tiegna, 2013). As could be seen, the analytical model is very fast compared to 3D FEA.

Table 2. Computation time comparison between analytical and FE-methods

Method	Number of nodes	Resolution time (excluding mesh and geometric construction)	Machine simulation
FEA made on Flux® 3D, with Magnetic scalar potential formulation, one time step, file size 322 Mo	1251790 (2nd order)	15 min 54 s	ASUS N773S Intel(R) Core (TM) i7-2670QM CPU@ 2.2.00GHz 2.2SHz, 12 Go RAM
Analytical model using 10 slices	-	45 s	

3.2. Mechanical analysis

3.2.1. Rotor deflection study

The rotor disk of an axial flux machine is exposed to electromagnetic forces acting on the axial direction which cause vibrations and distortion. As a result, the mechanical study is needed in order to avoid any possible friction between rotor and stator due to the deflection. Thus, the rotor disk should be thick enough to resist to axial forces. The axial forces F_{ax} acting on the rotor disk are calculated using the Maxwell stress tensor applied to the rotor surface. The expression of the axial force is given by Equation (11).

$$F_{ax} = \left[-\frac{\pi\left(R_o{}^2 - R_i{}^2\right)}{4\mu_0} \sum_{k\neq 0} \left(\left(C_k^{(2)}\right)^2 - \left(D_k^{(2)}\right)^2 + \left(E_k^{(2)}\right)^2 - \left(F_k^{(2)}\right)^2 \right) \right] \cdot \vec{e}_z \tag{11}$$

Figure 15 shows the waveform of the single side attraction force between the stator and the rotor at no load for an air gap equal to 1 mm. As shown, the rotor disk is subjected to a single side attraction force of 9,546 kN.

In the case of double stator, the rotor will be subject to two forces of attraction in opposite directions. Therefore, if the rotor is perfectly centred between the two stator disks then the force is equal to zero. However, for those small machines, having rotor perfectly balanced is not an easy task. Consequently, the resultant forces acting on the rotor disk vary in function of the off-centring as lastly illustrated and as in Table 3.

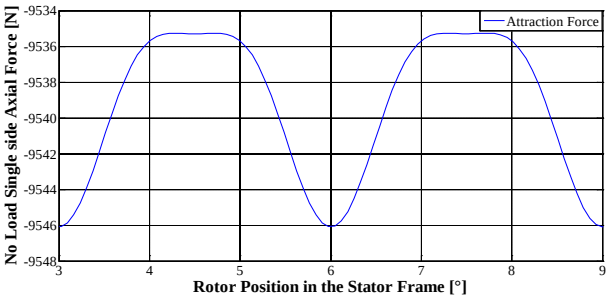

Figure 15. No load single side attraction force between disks

Table 3. Forces in function of the off-centering of the rotor disk

Off-centering	10	20	30	40	50	60	70	80	90
Force (N)	850	1700	2550	3430	4300	5210	6135	7089	8071

To overcome this centring defect, the rotor should be sized to satisfy the constraint of maximum off-centring tolerance. The support of the rotor structure, the junction with the shaft, and the applied axial force are described in Figure 16. This force is calculated for an off-centring tolerance equal to 10% and 20%. In practise, the accurate mechanical analysis of the rotor disk deflection should involve magneto-mechanical coupling, knowing that the axial resultant force varies in function of the deflection. On these terms the weak magneto-mechanical coupling is realised between the mechanical FE model and the analytical magnetic one, in order to be sure that the mechanical behaviour of the rotor disk could be demonstrated.

Since, the weak magneto-mechanical coupling had been assumed, so the structural analysis based on multi-static loads had been calculated step by step in function of the deflection, and carried out with the ANSYS FE-program coupled to the analytical magnetic model. The rotor deflection simulations were done for a fixed shaft and neglect the rotor rotation effects, eccentricity and unbalance, the calculation method for a circular disk is described according to (Yuang 1989; Parviainen, 2003; Abdel-Karim, 2008).

In fact, the rotor deflection study is based on a step by step calculation. First, for a given off-centering, the electromagnetic model computes the local forces applied on the rotor disk, after that the deflection will be computed via the mechanical model by assuming that the air gap is constant in every calculation step. For the next computation step the air gap thickness will be taken as the previous ones minus/plus the deflection distance for each air gap side. Then these locally calculated forces serve as an input for the mechanical model where they are distributed uniformly on the rotor core surfaces. Next, the rotor deflection is calculated and injected as an

input parameter in the electromagnetic model. This operation is repeated until the rotor disk reaches the static balance state or comes into contact with the stator.

In general, the deflection introduces an air gap eccentricity which can be static or dynamic or a mixed one. This eccentricity could cause a modulation of the stator phase currents with low frequency depending on the eccentricity type. For this type of machine, eccentricity fault is a very complex subject and 3D FE electromagnetic simulations of the complete geometry are needed. For this paper, the rotor disk deflection was studied in a static case in order to determine the rotor disk width minimum value avoiding its deflection due to attraction magnetic forces.

The flow chart of the weak coupling based magneto-mechanical analysis is illustrated in Figure 17, where th is the rotor thickness, small is the smaller air gap side, large is the bigger air gap side, F is the force, d is the deflexion i is the calculation step number and dt is the total deflection.

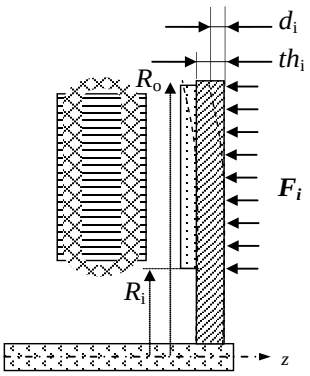

Figure 16. Rotor disk deflection due to the axial electromagnetic force

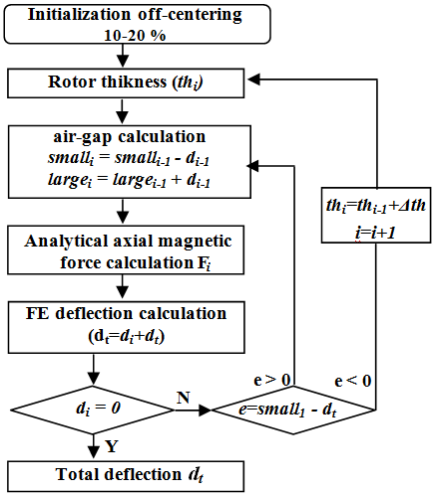

Figure 17. Flow chart of the weak coupling formulation

Figure 18 shows the rotor structures considered here. Its diameter is 360 mm whereas the shaft diameter is 40 mm. The rotor disk was fabricated using magnetic steel that have isotropic mechanical properties (the Young modulus $E = 210\,GPa$ and the Poisson's ratio $\nu = 0.3$). Obviously, the choice of hollowed rotor disk without reinforcement implies bigger thickness and consequently heavier rotor structure. However technical specification requires mass minimization without affecting performance. Indeed, the proposed machine has one rotor sandwiched between two stators. The flux passes from one stator to the other allowing for an ironless rotor (ideal balanced attraction forces case). The backing rotor steel

thickness could be then reduced. However, due the value of the one-side axial forces (20 kN), the rotor disk was made by a magnetic steel having a high elasticity limit that can resist to mechanical constraints. For higher benefit of this advantage, a second rotor structure type had been investigated, as shown in Figure 19, where the modified structure is presented. In this case the disk is hollowed and mechanical reinforcement was added to meet the constraint specifications.

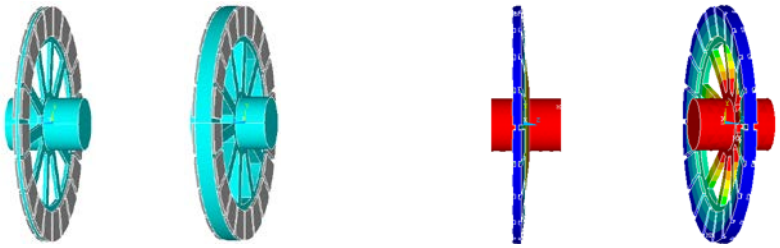

(a) Hollowed rotor disk for various thickness *(b) Example of rotor deflection*

Figure 18. First rotor structures

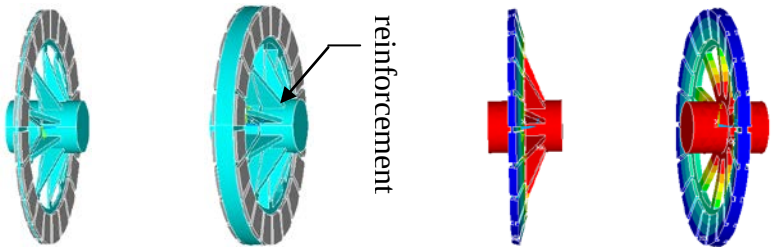

(a) Reinforced rotor disk for various thickness *(b) Example of rotor deflection*

Figure 19. Second rotor structures

The deflection in function of the force for both structures is presented in Figure 20. From this figure, it could be noted that to avoid any possible friction between the rotor and the stator for an off-centring of 10%, thickness of 10mm or more is satisfactory for the simple disc. However if the rotor is manufactured according to the second method, thickness of 5mm will satisfy this condition. In the case of an off-centring of 20%, thickness of 10mm for the simple disk and 6 mm for the reinforced one can be tolerated. As it could be seen, for both cases when the deformations are reasonable (on the order of few percent), the deformation is linear and obeys Hooke's law, therefore the rotor deformation remains in the elastic zone. Also, it could be noted that the deflection variation Δ_{def} decreases from one iteration *it* to another up to a value for which the force doesn't change anymore. This is due to the fact that the static balance (it_{eq}) between the three physical quantities force, deflection and elasticity is fulfilled.

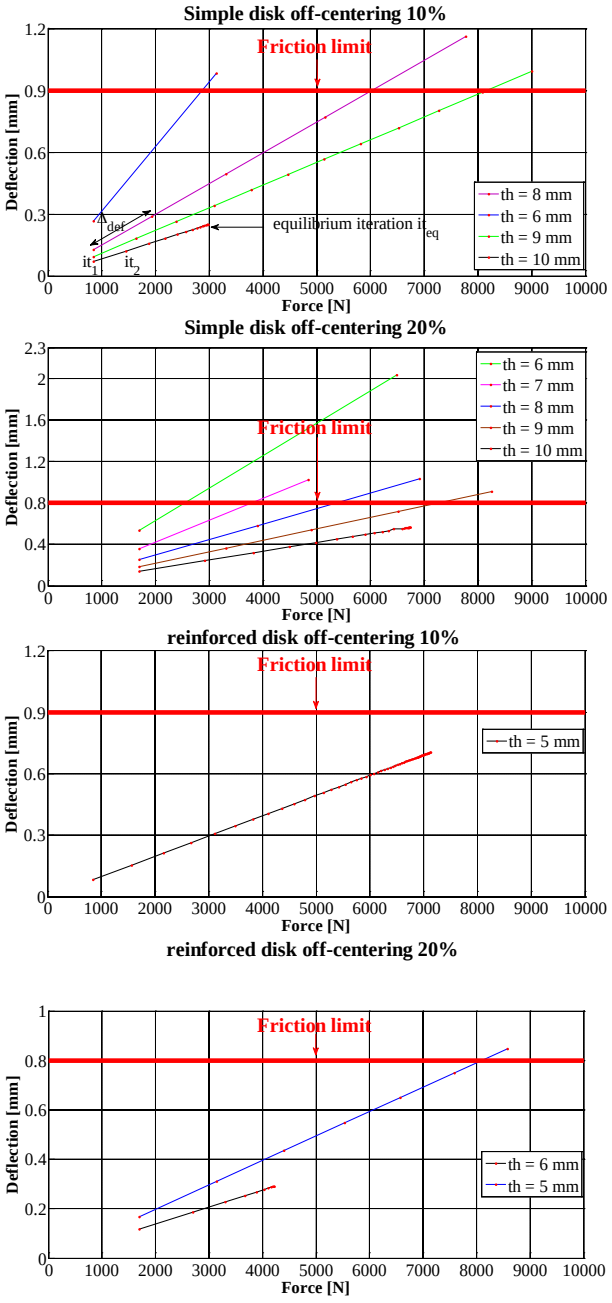

Figure 20. Rotor deflection versus the axial force

3.2.2. AFPM vibration behaviour

Noise and vibrations are considered as critical aspects in the integration of electrical machines in embarked environments. This makes that analyzing their vibration behaviour in the early stages of the design process an important issue. In this section, the magnetic computed forces on the air gap side stator surface are used as an input to determine the AFPM vibration behaviour. Thus, a structural 3D FE model is created to describe the vibration behavior of the machine.

The simulations were done for fixed end-bells sides and for 375 rpm machine's rated speed. The stator core laminations are taken into account using equivalent mechanical properties. By the same way, the windings with insulation are characterized by their equivalent mechanical properties. The end-windings, the end-bells and the frame are also considered in this study. The stator assembly is molded with perfect friction contact, without keys.

In a modal analysis the vibration modes can be obtained by solving the following matrix Equation (9) derived from the generalized equation of motion by assuming harmonic motion, free vibrations and ignoring the damping.

$$\left[[K] - \mathrm{w}^2 \cdot [\mathrm{M}]\right] \cdot \{\mathrm{U}\} = 0 \tag{9}$$

Otherwise, in the structural analysis, the structural dynamics equation is taken into account in the finite element dynamic matrix equation. Equation (10) gives the fully coupled finite element dynamic matrix equation.

$$[M]\{\ddot{\mathrm{U}}\} + [C] \cdot \{\dot{\mathrm{U}}\} + [\mathrm{K}]\{\mathrm{U}\} = \{\mathrm{f}\} \tag{10}$$

Where $[M]$, $[C]$ and $[K]$ are the mass, damping, and stiffness matrices, respectively, and $\{\mathrm{f}\}$ is the external force vector in the structure.

In order to develop the proposed model in this paper, some assumptions were formulated. First, only vibrations of electromagnetic origin are considered. The mechanical constraints are mainly localized on the air gap side stator surfaces. Finally, there is no rotor eccentricity and no rotor unbalance.

The modelling approach is established using a 3D FE mechanical structural model based on a modal superposition method built with commercial software ANSYS Mechanical®.

First the FE magnetic model is used to compute magnetic flux densities in the air gap on multiple radii of the stator air gap side faces. In our case 4 slices were considered (Ri ; Ri+(Ro-Ri)/3; Ri+2*(Ro-Ri)/3; Ro). Then the magnetic pressures components are derived via the Maxwell formalism (Figure 23) where Pn and Pt are respectively the normal and tangential magnetic pressure component and followed by a harmonic analysis.

Secondly the modal analysis is performed and the machine's vibrating modes are derived. A correlation between the natural frequencies of the structure and the harmonics of the magnetic pressure gives the possibly excited modes as for each harmonic frequency of the magnetic pressure correspond, or not, a natural frequency of the studied structure.

Finally, for those excited modes a structural analysis is performed in order to compute the dynamic displacements of each mode using sinusoidal wave form pressure as mentioned in Equation (12). The full diagram of the magneto-mechanic model of the proposed AFPM machine is given by Figure 21.

$$\begin{cases} P_n = \dfrac{dFn}{dS} = P_{\max} \cdot \cos(m\theta) \\ P_t = \dfrac{dFt}{dS} = P_{\max} \cdot \cos(n\theta) \end{cases} \tag{12}$$

Where m and n are respectively the circumferential and longitudinal modes number identified in the correlation phase and $P_{\max}$ is the maximal magnetic pressure value.

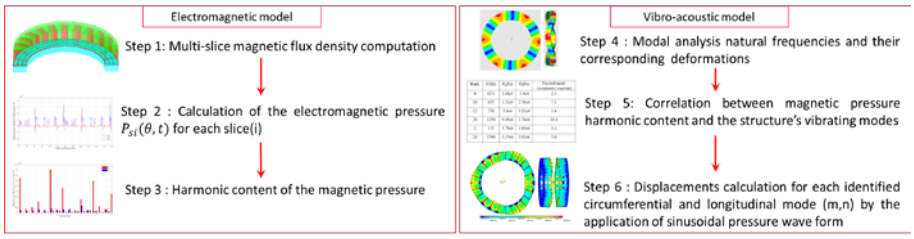

Figure 21. Full diagram of the magneto-structural vibration model

Chosen elastic moduli of the different materials are given in Table 4 where, E, G, ν and ρ are respectively Young modulus, shear modulus, Poisson's ratio and mass density. An exploded view of the modeled machine is presented in Figure 22.

Figure 22. Exploded view of the different structure elements

Table 4. Mechanical properties of the structure

Parameters	Laminations	Windings	Magnets	Frame
E_X (GPa)	200	9.4	160	71
E_Y (GPa)	200	9.4	160	71
E_Z (GPa)	0.8	9.4	160	71
G_{XY} (GPa)	79.3	3.5	64.5	26.7
G_{ZX} (GPa)	0.3	3.5	64.5	26.7
G_{YZ} (GPa)	0.3	3.5	64.5	26.7
ν_{XY}	0.3	0.35	0.24	0.33
ν_{ZX}	0.0012	0.35	0.24	0.33
ν_{YX}	0.0012	0.35	0.24	0.33
ρ (kg.m^{-3})	7700	8890	7500	2700

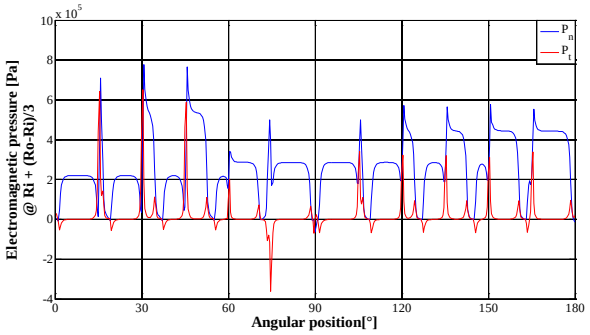

Figure 23. Predicted FE air gap pressure components

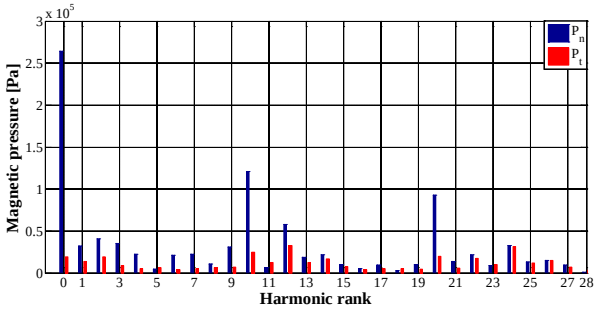

Figure 24. Harmonic content of the air gap force density components

The magnetic pressure harmonic analysis is given in the Figure 24. The highest amplitudes harmonics are the k*Nr, k ϵ IN harmonic numbers. The harmonic of rank 1 is responsible for unbalanced magnetic force since it tends to misalign the stator from the axis of rotation. As expected, the tangential component of the force is globally much lower than the normal component. The correlation between the structure natural frequencies, and the harmonics of the magnetic pressure makes that the modes presented in Table 5 are mostly excited. The investigation of those modes gives the dynamic displacements presented in Figure 25. The maximum displacement U_{max} value is about 0.057 μm.

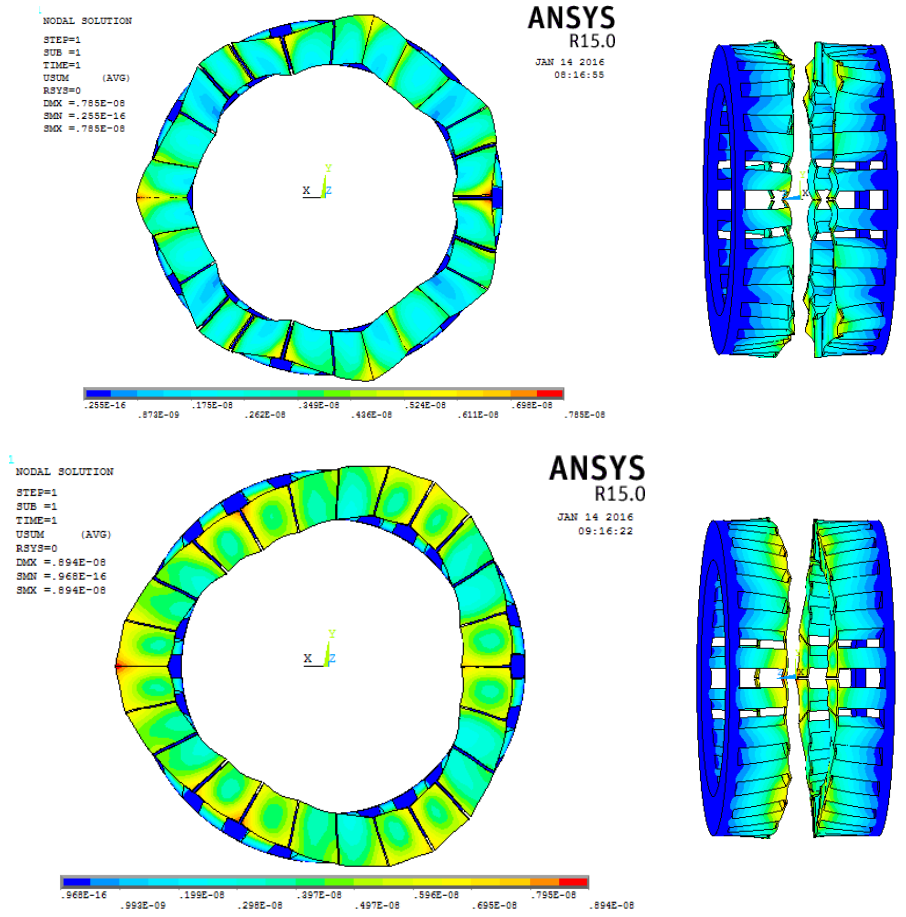

Figure 25. Mapped displacements for Mode (7,3) and mode (3,4)

Table 5. Principal exited vibrating modes and their corresponding pressure and displacements

Rank	F(Hz)	P_n(Pa)	P_t(Pa)	Excited mode (Circumferential, Longitudinal)	U_{max} (m)
1	62.5	2.68e5	1.8e4	2,1	0.127e-7
10	625	1.21e5	2.36e4	7,3	0.785e-8
12	750	5.8e4	3.11e4	3,4	0.894e-8
20	1250	9.45e4	1.76e4	10,4	0.538e-8
2	125	3.79e4	1.83e4	3,1	0.536e-8
24	1500	3.15e4	3.02e4	5,6	0.738e-8
3	187.5	3.54e4	8.25e3	3,2	0.29e-8
9	562.5	3.26e4	6.64e3	6,3	0.22e-8
14	875	1.8e4	1.63e4	4,5	0.423e-8

3.3. Lumped parameter thermal model

The study of the thermal behaviour and consequent cooling requirements is mandatory in the design stage. An exact prior determination of the machine thermal behaviour is very difficult due to many factors such as the exact evaluation of the loss components and their distribution, the three dimensional complexity of the problem and the lack of information about convection coefficients. Therefore, the Lumped Parameter Thermal Model (LPTM) is widely used in the early stage of the design. It consists of thermal resistances, capacitances and heat sources network. The temperatures are the quantities to be estimated in each node. This model is essentially an analogy of an electrical circuit in which the heat flowing in each part of the circuit is given by temperature difference divided by thermal resistance. These thermal resistances depend on the material characteristics, their geometrical dimension, and especially on the heat transfer nature as reminded by (Vasilescu, 2002; Abdel-Karim, 2008; F. Marignetti *et al*., 2008; Verez *et al*., 2012).

So, the network of thermal resistances is built by subdividing the machine geometry into small volumes that are considered to be homogeneous and isotherm, and thus it is possible to draw energy balance up for each node related to a given region. The connection between different volumes applied to the axial flux machine is presented in Figure 26.

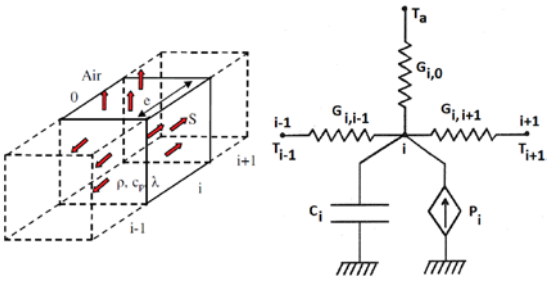

Figure 26. Conductance network

The heat equation is given in (13) for an infinitesimal volume.

$$\rho \cdot \mathrm{c} \frac{\mathrm{dT}}{\mathrm{dt}} \cdot d\tau + \nabla \Phi \cdot d\tau = p d\tau \tag{13}$$

Where, $\rho \cdot \mathrm{c} \cdot \mathrm{dT}/\mathrm{dt}$ represents the rate of stored energy change in infinitesimal volume, where $d\tau \cdot \rho$ is the density, and c is the specific heat capacity. The second element of the equation is the flux outgoing $d\tau$, and the third element is the heat production density p produced in this volume. The different thermal conductance expression is given in (Abdel Karim, 2008; Verez *et al.*, 2012; Tiegna, 2013).

In order to check the model consistency, comparative study had been performed between the exposed LPTM and 3D FEA. Results show that the analytical model gives good results for both transient – and steady-state (Figure 27). Table 6 shows the steady state results obtained in both simulations (Verez *et al.*, 2012). The time taken to reach steady-state in this case is approximately 167 minutes.

Table 6. Simulation results for steady-state

Region	LPTM Temperatures (°C)	3D FEA Temperatures (°C)
Conductors inside stator slots	110	108
External air gap	98	98
Stator Yoke	94	96
Frame	93	87

The obtained temperatures are close to each other. Conductors and the frame are 2°C and 6°C, respectively hotter with the analytical method than values obtained with the numerical simulation, but the stator yoke is 2°C colder (Verez *et al.*, 2012).

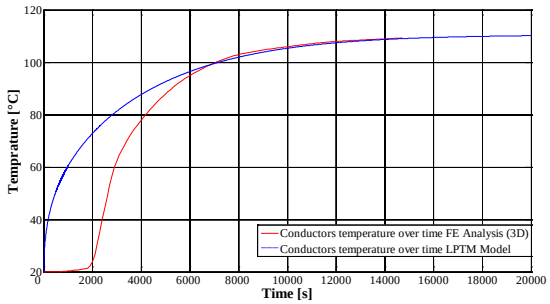

Figure 27. Conductors temperature over time comparison

4. Machine test and experimental results

The AFPM generator prototype has been constructed and tested (Tiegna, 2013). Hence, the obtained measurements are compared to those calculated by the analytical magnetic model. Figure 28 shows experimental and analytical EMF waveforms at 375 rpm. They are in close agreement with the ones predicted by the analytical model. Figure 29 shows the EMF phase amplitude variation with the mechanical rotation speed. In average, the measured EMF is 9% lower than the one obtained by analytical model. This difference is expected, since the analytical simulation was made with the main assumption that the permeability of the magnetic material is infinite. So, as explained above, this difference between measured and calculated EMF is mainly due to the additional air gaps between stator teeth and to a lesser extent to saturation. The three stator phase EMFs at no load are perfectly balanced.

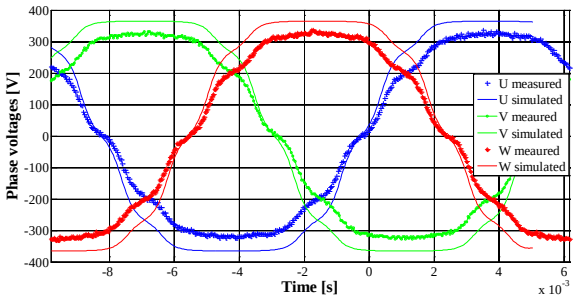

Figure 28. Comparison between the measured and the analytically calculated EMFs at no load

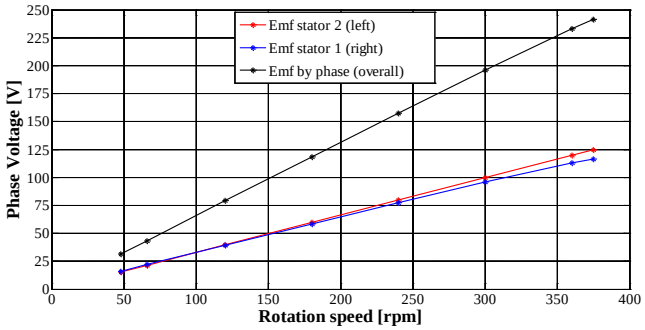

Figure 29. Measured EMFs at no load

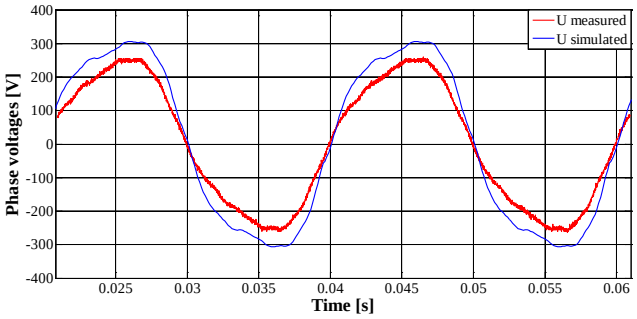

Figure 30. Measured and analytically simulated line to neutral stator phase voltage for 50Hz and generator operation at resistive load (P=4.8kW)

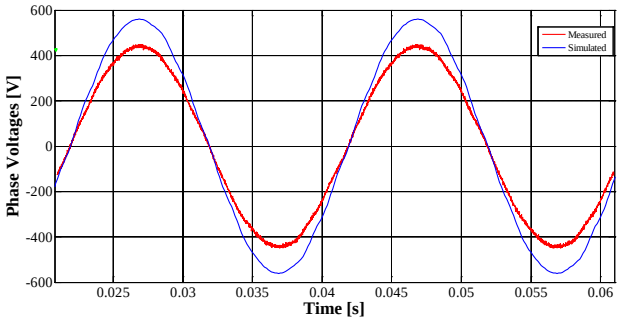

Figure 31. Measured and analytically simulated line to line stator phase voltage for 50Hz and generator operation at Resistive load (P=4.8kW)

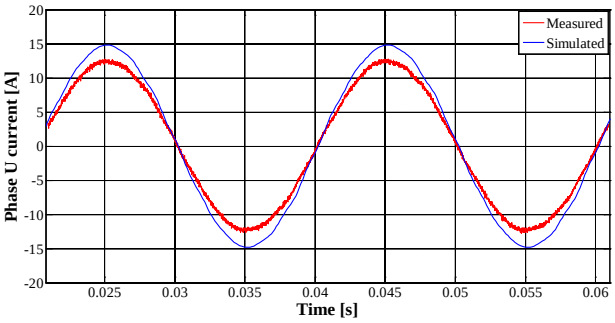

Figure 32. Measured and analytically simulated stator phase Current for 50 Hz and generator operation at resistive load (P=4.8kW)

The machine, operated as a generator, it had been tested with purely three phase resistive load. As a result, Figures 30 and 31 show respectively the comparison between simulation and measurement results of the stator phase line to neutral U voltage and line to line stator voltage. The saturation effect causes a third harmonic in the line to neutral stator phase voltages. This third harmonic distorts the line to neutral stator phase voltage waveform. The measured lines to neutral stator phase voltages are given in Figure 30 and they seem to be balanced.

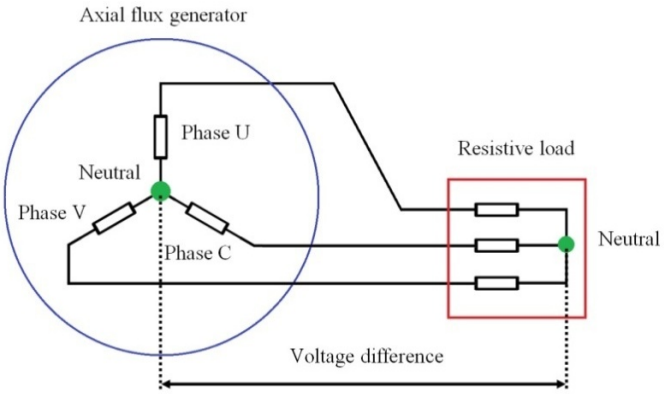

Figure 33. Setup for generator resistive loading

Figure 32 shows the line current. Even though, when the load is purely resistive, it could be noted that the generator phase voltage and the line current do not have the same waveform shape. This is due to the fact that the neutral point of the generator armature windings is not connected to the neutral point of the resistive load (Figure 33). There is a voltage difference between neutral points of the

generator's armature windings and the resistive load. The speed was imposed to have 50 Hz electric frequency.

Table 7. Inductances calculation results

Cyclic inductance (mH)	Analytical model	Measured
	15.1	13.2

Table 8. Machine performance

Iron losses (W)	355
Joule losses (W)	713.6
Mechanical losses (W)	10
Efficiency	90.3%
Power factor	$\cos(\varphi) = 0.9857$

The measured voltages (Figure 30) are approximately 16% lower than the simulated values. It is a reasonable decreasing, since in addition to magnetic saturation, end effects are also neglected in analytical simulations. The comparison between cyclic inductances estimated using analytical model (end windings are not considered) and the measured values are presented in Table 7. The measurements match fairly well with analytical results. Table 8 gives the main performances, where efficiency and power factor calculation are based on the on-load line to line voltage and stator phase current.

5. Conclusion

In this research, general analysis of an analytical design appoach of semi-closed slotted axial flux permanent magnet synchronous generator for wind turbine had been presented. The proposed analysis is based on the combination between analytical magnetic model, mechanical structural rotor deflection study, and lumped parameter thermal model.

The analytical magnetic model is used to analyse the designed structure, which is based on quasi-3D analytical approach using multi-slice technique. The magnetic field distribution in each slice is derived from an exact 2D solution of the Maxwell equations thanks to the separation of variables method. Good agreements had been reached between analytical open circuit performance and those obtained by 3D FEA.

The mechanical rotor deflection study allows choosing the disk structure and thickness for a given tolerated off-centring. Furthermore, a 3D FE mechanical

structural model based on a modal superposition method was developed to provide for a given speed profile, the magnetic induction, the electromagnetic torque, as well as the vibrating modes and dynamic displacements.

The lumped parameter thermal model was developed using simple isotherm volumes. This model allows fast computation of the machine thermal behaviour.

As well as to get manufacturing expertise, and to verify the validity of the analysis tool, hence a prototype had been constructed and experimental measurements of EMF, stator phase voltages, line to line stator voltages, stator phase currents, and inductances had been conducted. Good agreements between simulated and measured waveforms had been obtained. From the comparison, it's possible to evaluate the performance of the AFPM machine with reasonable accuracy via the proposed model.

Bibliography

Abdel-Karim N. (2008). *Dimensionnement et optimisation d'un aérogénérateur à aimants permanents à flux axial de petite puissance*. Ph. D thesis (French) from University of Le Havre

Abdel Karim N., Azzouzi J., Barakat G. (2006). Winding functions theory and Maxwell's equations coupled analytical modeling of an axial flux PM synchronous machine. *International Revue of Electrical Engineering (IREE)*, vol. 1, n° 1, p. 27-35.

Amara Y., Reghem P., Barakat G. (2010). Analytical prediction of eddy-current loss in armature windings of permanent magnet brushless AC Machines. *IEEE Transactions on Magnetics*, vol. 46, n° 8, p. 3481-3484.

Azzouzi J. (2007). *Contribution à la modélisation et à l'optimisation des machines synchrones à aimants permanents à flux axial. Application au cas de l'aérogénérateur*. Ph. D thesis (French) from University of Le Havre.

Azzouzi J., Barakat G., Dakyo B. (2005). Quasi-3-D analytical modeling of magnetic field of an axial flux permanent-magnet synchronous machine. *IEEE Energy Conversion*, vol. 20, n°. 4, p. 746-752.

Barakat G., El Meslouhi T. and Dakyo B. (2001). Analysis of the cogging torque behaviour of a two-phase axial flux permanent magnet synchronous machine. *IEEE Transactions on Magnetics*, vol. 37, n° 4, p. 2803-2805.

Barakat G. and Amara Y. (2011). Analytical modeling of flat and tubular linear PM machines with surface-mounted magnets and semi-closed slots. *in Proceeding of International Symposium on Linear Drives for Industry Applications* LDIA 2011, Eindhoven, Netherlands.

Bellara A., Amara Y., Barakat G., Reghem P.. (2010). Analytical modeling of the magnetic field in axial flux permanent magnet machines with semi-closed slots at no load, *in Proceeding of the XIXe International Conference on Electrical Machines ICEM 2010*, Rome, Italy.

Cvetkovski G., Petkovska L., Cundev M., Gair S.. (2000). Quasi 3D FEM in function of an optimization analysis of a PM disk motor. *in Proceeding of the International Conference on Electrical Machines ICEM 2010,* vol. 5, Helsinki, p. 1871-1875.

de la Barrière O., S. Hlioui, H. Ben Ahmed, M. Gabsi, M. LoBue. (2010). Three-dimensional analytical modeling of a permanent-magnet linear actuator with circular magnets. *IEEE Transactions on Magnetics,* vol. 46, n° 9, p. 3608-3616.

Dhifli M., Bali H., Laoubi Y., Verez G., Amara Y., Barakat G. (2014). Modeling and Prototyping of Axial Flux Permanent Magnet Machine for Small Wind Turbine. *in Proceeding of Electrical Sciences and Technologies in Maghreb CISTEM'14,* Tunis, Tunisia.

Furlani E.P., Knewtson M.A. (1997). A three-dimensional field solution for permanent magnet axial-field motors. *IEEE Transactions on Magnetics,* vol. 33, n° 3, p. 2322-2325.

Gieras J.F., Wang R.J., Kamper M.J. (2008). *Axial Flux Permanent Magnet Brushless Machines,* Springer Verla.

Gysen B. L. J., Jansen J. L. G., Paulides J. J. H., Lomonova E. A. (2009). Design aspects of an active electromagnetic suspension system for automotive applications. *IEEE Transactions on Magnetics,* vol. 45, n° 5, p. 1589-1597.

Hemeida A., Sergeant P. (2014). Analytical Modelling of Surface PMSM Using a Combianed Solution of Maxwell's Equations and Magnetic Equivalent Circuit (MEC). *IEEE Transactions on Magnetics,* DOI 10.1109/TMAG.2014.2330801.

Lubin T., Mezani S., Rezzoug A. R. (2011). 2-D analytical model for surface-mounted permanent-magnet motors with semi-closed slots. *IEEE Transactions on Magnetics,* vol. 47, n° 2, p. 479-492.

Mahmoudi A., Rahim N. A., Hew W. P. And Uddin M. N. (2008). Design, analysis, and prototyping of a novel-structured solid-rotor-ringed line-start axial-flux permanent-magnet motor. *IEEE Transactions. on Industrial. Electronics,* vol. 55, n° 10, p. 3591-3601.

Marignetti F. and Colli V. D. (2008). Design of Axial Flux PM Synchronous Machine Through 3-D Coupled Electromagnetic Thermal and Fluid-Dynamical Finite-Element Analysis. *IEEE Transactions. on Industrial. Electronics,* vol. 61, n° 4, p. 1722-1734.

Parviainen A. (2003). *Design of axial flux PM low speed machines and performance comparison between radial flux and axial flux machines.* PhD thesis,Lappeenranta University of Technology.

Parviainen A., Niemelä M. and Pyrhönen J. (2004). Modeling of axial flux permanent magnet machines. *IEEE Transactions. Industry. Applications,* vol. 40, n° 5, p. 1333-1340.

Seo J. M., Ro J. S., Rhyu S. H., Jung I. S. and Jung H. K. (2015). Novel Hybrid Radial and Axial Flux Permanent-Magnet Machine Using Integrated Windings for High-Power Density. *IEEE Transactions on Magnetics,* DOI 10.1109/TMAG.2014.2344044.

Shin P. S., H. J. Cheung. (2011). A Magnetostrictive Force and Vibration Mode Analysis of 3 kW BLDC Motor by a Magneto-Mechanical Coupling Formulation. *Journal of Electrical Engineering & Technology,* vol. 6, n° 1, p. 76-80.

Tiegna H.. (2013). *Contribution à la modélisation analytique des machines synchrones à flux axial à aimants permanents à attaque directe en vue de leur dimensionnement.* Ph. D thesis (French) from University of Le Havre.

Tiegna H., Bellara A., Amara Y., Barakat G. (2012). Analytical Modeling of the Open-Circuit Magnetic Field in Axial Flux Permanent Magnet Machines with Semi-Closed Slots. *IEEE Transactions on Magnetics*, vol. 48, n° 3, p. 1212-1226.

Tiegna H., Amara Y. and Barakat G. (2011). Multislice analytical model of axial flux PM machines. *in Proceeding of* COMPUMAG 2011, Sydney, Australia.

Verez G., Tiegna H., Barakat G. and Hoblos G.. (2012). Analytical Thermal Modelling of Axial Flux Permanent Magnet Synchronous Machines, *in Proceeding of the XIX International Conference on Electrical Machines ICEM 2012*, Marseille, France.

Zhu Z. Q., Ruangsinchaiwanich S., Ishak D. and Howe D. (2005). Analysis of cogging torque in brushless machines having nonuniformly distributed stator slots and stepped rotor magnets. *IEEE Transactions on Magnetics*, vol. 41, n° 10, p. 3910-3912.

Wang J., Jewell G.W. andHowe D. (2001). Design optimisation and comparison of tubular permanent magnet machine topologies. *Electric Power Applications IEE Proceedings*, vol. 148, n° 5, p. 456-463.

Wu L. J., Zhu Z. Q., Staton D., Popescu M. and Hawkins D. (2011). Subdomain model for predicting armature reaction field of surface-mounted permanent-magnet machines accounting for tooth-tips. *IEEE Transactions on Magnetics*, vol. 47, n° 4, p. 812-822.

Zhilichev Y. N. (1998). Three-dimensional analytic model of permanent magnet axial flux machine. *IEEE Transactions on Magnetics*, vol. 34, n° 6, p. 3897-3901.

Annex

For a given slice having R_m as a mean radius, the general solution of these equations can be expressed for a region 'i' by:

$$A_r^{(i)}(\varphi,z) = A_{rp}^{(i)}(\varphi,z) + a_0^{(i)} + \sum_{k=1}^{+\infty} \frac{R_m}{k\lambda} \left\{ \begin{array}{l} \left[C_k^{(i)} \mathrm{ch}\left(\frac{k\lambda}{R_m} z\right) + D_{nk}^{(i)} \mathrm{sh}\left(\frac{k\lambda}{R_m} z\right) \right] \cos(k\lambda\varphi) \\ + \\ \left[E_k^{(i)} \mathrm{ch}\left(\frac{k\lambda}{R_m} z\right) + F_k^{(i)} \mathrm{sh}\left(\frac{k\lambda}{R_m} z\right) \right] \sin(k\lambda\varphi) \end{array} \right\} \quad (11)$$

The magnetic field vector components can be expressed in each region as follows.

Region I (slots)

$$B_\varphi^{(I,l)}(\varphi,z) = -\mu_0 J^{(l)}\left(z + h_b + h_s\right) + \sum_{m\neq 0} f_m^{(I,l)} \frac{\sinh\left[\frac{m\pi}{R_m w_s}(z + h_b + h_s)\right]}{\cosh\left(\frac{m\pi}{R_m w_s}\left(h_b + h_s\right)\right)} \times \cos\left[\frac{m\pi}{w_s}(\varphi - \varphi_{ll})\right] \quad (12)$$

$$B_z^{(I,l)}(\varphi,z)=\sum_{m\neq 0} f_m^{(I,l)}\frac{\cosh\left[\dfrac{m\pi}{R_m w_s}(z+h_b+h_s)\right]}{\cosh\left(\dfrac{m\pi}{R_m w_s}(h_b+h_s)\right)}\times\sin\left[\frac{m\pi}{w_s}(\varphi-\varphi_{I,l})\right] \tag{13}$$

Region II (slot opening area)

$$B_\varphi^{(II,l)}(\varphi,z)=\sum_{m\neq 0}\left[C_m^{(II,l)}\frac{\sinh\left(\dfrac{m\pi}{R_m w_o}z\right)}{\cosh\left(\dfrac{m\pi}{R_m w_o}h_b\right)}+D_m^{(II,l)}\frac{\cosh\left(\dfrac{m\pi}{R_m w_o}z\right)}{\cosh\left(\dfrac{m\pi}{R_m w_o}h_b\right)}\right]\times\cos\left[\frac{m\pi}{w_o}(\varphi-\varphi_{II,l})\right]-\mu_0 J^{(l)}\frac{w_s}{w_o}h_s \tag{14}$$

$$B_z^{(II,l)}(\varphi,z)=\sum_{m\neq 0}\left[C_m^{(II,l)}\cosh\left(\frac{m\pi}{R_m w_o}z\right)+D_m^{(II,l)}\sinh\left(\frac{m\pi}{R_m w_o}z\right)\right]\times\sin\left[\frac{m\pi}{w_o}(\varphi-\varphi_{II,l})\right] \tag{15}$$

Region III (mechanical air gap)

$$B_\varphi^{(III)}(\varphi,z)=\sum_{k\neq 0}\left\{\left[C_k^{(III)}sh\left(\frac{k\lambda_p z}{R_m}\right)+D_k^{(III)}ch\left(\frac{k\lambda_p z}{R_m}\right)\right]\cos(k\lambda_p\varphi)+\left[E_k^{(III)}sh\left(\frac{k\lambda_p z}{R_m}\right)+F_k^{(III)}ch\left(\frac{k\lambda_p z}{R_m}\right)\right]\sin(k\lambda_p\varphi)\right\} \tag{16}$$

$$B_z^{(III)}(\varphi,z)=\sum_{k\neq 0}\left\{\left[C_k^{(III)}ch\left(\frac{k\lambda_p z}{R_m}\right)+D_k^{(III)}sh\left(\frac{k\lambda_p z}{R_m}\right)\right]\sin(k\lambda_p\varphi)-\left[E_k^{(III)}ch\left(\frac{k\lambda_p z}{R_m}\right)+F_k^{(III)}sh\left(\frac{k\lambda_p z}{R_m}\right)\right]\cos(k\lambda_p\varphi)\right\} \tag{17}$$

Region IV (PM region)

$$B_\varphi^{(IV)}(\varphi,z)=\sum_{k\neq 0}\left[\sinh\left(\frac{k\lambda_p z}{R_m}\right)-\tanh\left(\frac{k\lambda_p(h_a+e)}{R_m}\right)\cosh\left(\frac{k\lambda_p z}{R_m}\right)\right]\times\left[C_k^{(IV)}\cos(k\lambda_p\varphi)+E_k^{(IV)}\sin(k\lambda_p\varphi)\right] \tag{18}$$

$$B_z^{(IV)}(\varphi,z)=\left[\sum_{k\neq 0}\left(\begin{array}{l}\left[C_k^{(IV)}\left\{\begin{array}{l}-\tanh\left(\dfrac{k\lambda_p(h_a+e)}{R_m}\right)\sinh\left(\dfrac{k\lambda_p z}{R_m}\right)\\ +\cosh\left(\dfrac{k\lambda_p z}{R_m}\right)\end{array}\right\}+F_k^M\right]\times\sin(k\lambda_p\varphi)\\ -\left[E_k^{(IV)}\left\{\begin{array}{l}\cosh\left(\dfrac{k\lambda_p z}{R_m}\right)-\tanh\left(\dfrac{k\lambda_p(h_a+e)}{R_m}\right)\\ \sinh\left(\dfrac{k\lambda_p z}{R_m}\right)\end{array}\right\}-E_k^M\right]\times\cos(k\lambda_p\varphi)\end{array}\right)\right] \tag{19}$$

A set of linear Equations (20) and (21), where coefficient of magnetic field solution in region III are the unknowns, is obtained after combining equations and treatment of boundary and interface conditions

$$C_k^{(III)}\tanh\left(\frac{k\lambda_p(h_a+e)}{R_m}\right)-\sum_{n\neq 0}C_n^{(III)}\times\Re(n,k,-)=\left\{\begin{array}{l}\left(F_k^M\cos(k\lambda_p\theta)+E_k^M\sin(k\lambda_p\theta)\right)\\ \cdot\left(\tanh\left(\frac{k\lambda_p(h_a+e)}{R_m}\right)\cosh\left(\frac{k\lambda_p e}{R_m}\right)-\sinh\left(\frac{k\lambda_p e}{R_m}\right)\right)\\ +\frac{2\mu_0 h_s w_s}{\pi}\frac{\sin\left(k\lambda_p\frac{w_o}{2}\right)}{kw_o}\sum_{l=0}^{\frac{N_s}{\lambda_p}-1}J^{(l)}\cos\left(k\lambda_p\frac{2\pi l}{N_s}\right)\end{array}\right\} \quad (20)$$

$$E_k^{(III)}\tanh\left(\frac{k\lambda_p(h_a+e)}{R_m}\right)-\sum_{n\neq 0}E_n^{(III)}\times\Re(n,k,+)=\left\{\begin{array}{l}\left(F_k^M\sin(k\lambda_p\theta)-E_k^M\cos(k\lambda_p\theta)\right)\\ \cdot\left(\tanh\left(\frac{k\lambda_p(h_a+e)}{R_m}\right)\cosh\left(\frac{k\lambda_p e}{R_m}\right)-\sinh\left(\frac{k\lambda_p e}{R_m}\right)\right)\\ +\frac{2\mu_0 h_s w_s}{\pi}\frac{\sin\left(k\lambda_p\frac{w_o}{2}\right)}{kw_o}\sum_{l=0}^{\frac{N_s}{\lambda_p}-1}J^{(l)}\sin\left(k\lambda_p\frac{2\pi l}{N_s}\right)\end{array}\right\} \quad (21)$$

Received: 22 June 2015
Accepted: 21 March 2016